Stimulation-artifact-free, high-spatiotemporal-resolution *in vivo* optoEphys with μLED optoelectrodes

Kanghwan Kim, Mihály Vöröslakos, John P. Seymour, Kensall D. Wise, György Buzsáki, and Euisik Yoon

Abstract

In vivo extracellular electrophysiology and genetic-engineering-assisted optical stimulation combined (*in vivo* optoEphys) has proven its great potential to be one of the best tools for study of the intricate networks inside the brain. Micro-LED optoelectrode, the Michigan Probe with monolithically integrated cell-sized LEDs, enabled *in vivo* optoEphys at the highest spatial resolution to date. However, high-magnitude stimulation artifact had prevented experiments from being conducted at a desirably high temporal resolution. Here, we report engineering schemes with which the magnitude of stimulation artifact generated from μLED optoelectrode can be greatly reduced for nearly artifact-free *in vivo* experiments. The second-generation μLED optoelectrodes, fabricated using heavily boron-doped silicon wafer and equipped with dedicated EMI shielding layers, exhibited capability to record neuronal activities during fast-switched optical stimulations without degradation in signal quality. We believe that the novel μLED optoelectrodes will lead to exciting discoveries of the brain's circuit-level mechanisms.

Introduction

Neurons talk with one another using pulses of electricity. While neuronal communication involves change in the electric potential inside the cell body, since neurons are suspended in highly conductive media, observation of the change in the electrical field from locations outside of the cell provides sufficient information about the communication taking place among the cells. Characterization of such communication; including the wiring pattern, intensity of the connection, time-domain correlation between two communicating neurons' firing pattern, etc; inside a volume of tissue in which a number of neurons are densely populated requires multiple recording electrodes to be located in

vicinity of one another so that activities of multiple neurons can be simultaneously recorded [Buzsaki 2004].

Analysis of a complicated system, such as a network of densely populated neurons inside a part of a brain, requires capabilities not only to accurately monitor the system's activity as a whole but also to precisely modulate the system's activity at specific locations. Among many techniques that allow modulation of neuronal activities, optogenetics has become the most widely adopted technique thanks to its advantages over the other techniques: cell type specificity and high temporal resolution [Boyden 2005] [Deisseroth 2011]. The combination of genetic engineering-assisted optical stimulation and high-resolution electrical recording of neuronal activities, here termed opto-electrophysiology (optoEphys), has proven to be one of the best tools for study of the intricate networks inside the brain [Buzsaki 2015].

Neuroscientists and engineers together have developed a number of tools that can provide the very capability to electrically record the activity of a set of neurons at high spatial resolution while optically stimulating a portion of the neurons. Implantable silicon multi-electrode arrays, or Michigan probes [Wise 1975] [Wise 2008], has been one of the best candidates to provide the capability thanks to its planar profile and standardized fabrication process. A number of devices that took advantage of the Michigan probe platform had been developed and utilized for interesting neuroscience discoveries [Wu 2013] [Kampasi 2016]. Among those is micro-LED (μLED) optoelectrode, the Michigan probe with monolithically integrated cell-sized LEDs for optical stimulation [Wu 2015], shown in Fig. 1a. This device, thanks to the small size of the light source and the small profile of the device, enabled *in vivo* optical stimulation of neurons in the brains of moving animals at the highest spatial resolution reported to date, combined with simultaneous recording of activities of the very neurons that are under the influence of the optical stimulation. A number of interesting discoveries have been made since inception of device [Wu 2015] [English 2017].

While being considered very promising, μLED optoelectrode had not been utilized at its full capacity; the optoelectrode was not able to provide stimulating and recording capacities both at high spatiotemporal resolutions, due to existence of high-magnitude stimulation artifact in the recorded signal during optical stimulation [Wu 2015] [Kim 2016]. While the recording channels were supposed to exclusively pick up neuronal activities in the vicinity of the recording electrodes, signals that resemble the signal provided to the LEDs for optical stimulation (Fig. 1e) showed up on the recorded signals. Because of existence of the stimulation artifact, either the optical stimulation had to be limited to slowly-changing low-frequency signal, or the signals collected within a few milliseconds around the beginning and the ending of pulsed optical simulation had to be discarded from the recorded neural data. Because both of these measures prevent application of fast-switching pulsed optical stimulation, the temporal resolution of the stimulation had been limited to at most a couple of tens to hundreds of hertzs. The limited temporal resolution of stimulation in turn prevented use of the μLED optoelectrodes in wider applications in which high temporal resolution is required, for example in closed-loop experimental setups in which the stimulation is required to be applied right after detection of a certain activity in the recorded signal [Grosenick 2015].

A variety of forms of optical-stimulation-induced artifact on signals recorded *in vivo* using electrode arrays have been reported in the literature [Wise 1970] [Royer 2010] [Mikulovic 2016] [Jun 2017] [Kampasi 2016] [Kampasi 2018] [Ayling 2009] [Han 2009] [Cardin 2010], [Khurram 2013] [Laxpati 2014] [Budai 2018]. Among them is artifact due to photoelectrochemical effect (PEC), which is emission of electrons from the surface of metal at the metal-electrolyte interface. Because it takes place when a metal electrode is exposed to incident photons with sufficient energy, PEC has been observed in a variety of devices regardless of the substrate material [Ayling 2009] [Han 2009] [Cardin 2010], [Khurram 2013] [Laxpati 2014] [Budai 2018]. Another form of stimulation artifact is that resulting from electromagnetic interference (EMI), a phenomenon that takes place due to exchange of electrical and

magnetic energy between two adjacent conductive materials that carry electricity via capacitive and inductive coupling. Because EMI takes place when the source (or the aggressor) is in close proximity to the target (or the victim), it has been observed on a device that have light sources directly integrated on the recording device itself [Kampasi 2018]. Finally, artifact that was induced by photovoltaic (PV) effect, during which the electrostatic potential of the semiconductor substrate changes due to illumination by photons with sufficient energy, has been observed. Because most high-density *in vivo* extracellular electrode arrays have been made using silicon substrate, the artifact was observed in many experiments in which visible light ($\lambda < 1100$ nm) was used [Mikulovic 2016] [Jun 2017]. A variety of engineering measures has taken place to prevent the artifact from arising, including replacement of metal electrodes with transparent electrodes [Kuzum 2014], [Park 2016], inclusion of EMI shielding structures [Kampasi 2018], and degenerate doping of the silicon substrate [Wise 1970] [Scholvin 2016]. Unfortunately, because the μLED optoelectrodes is made up of heterogeneous materials that are highly densely integrated within a small footprint, neither had the sources of the artifact in μLED optoelectrodes been clearly identified nor had the solutions for elimination of these artifact been suggested yet.

We identified the sources of stimulation artifact on the μLED optoelectrode and successfully reduced the stimulation artifact to be less than 50 μV peak-to-peak (pp) on all the recording channels during pulsed optical stimulation *in vitro*. The sources of stimulation artifact include EMI from LED driving signal (Fig. 1c) and PV-induced electrostatic potential from illumination on the silicon substrate (Fig. 1d). PEC-induced stimulation artifact, on the other hand, turned out to be insignificant on μLED optoelectrodes because the amount of photons that are incident on metal-electrolyte interface is negligible. We studied the mechanisms by which the components of the artifact are generated and successfully reduced the effect by implementing engineering schemes. The second-generation μLED optoelectrode (Fig. 1f) fabricated with both EMI- and PV- reduction schemes (Figs. 1g and 1h, respectively) achieved reduction of stimulation artifact magnitude to nearly zero on most of the

recording channels (Fig. 1i), and lower than 50 μVpp on all the recording channels with additional pulse slew rate modification. By confirming that stimulation artifact can be successfully eliminated *in vivo*, we provided evidence that the μLED optoelectrodes are capable of truly high-spatiotemporal-resolution *in vivo* optoEphys.

Results

Reduction of EMI-induced artifact with shielding

The shape of the stimulation artifact recorded on the 1st-generation μLED optoelectrode (Fig. 1e) resembles that of the voltage signal provided to the μLEDs for optical stimulation. This resemblance suggests that the LED driving signal becomes coupled to the signal recording circuitry as a result of EMI. As shown in Fig. 2a and Fig. 2b, on μLED optoelectrode, the LED driving signal is delivered through metal traces (interconnects) that connect the μLEDs to the backend of the optoelectrode. The signal recording circuitry, including the metal electrodes and the interconnects that connect the electrodes and backend of the electrode, is integrated on the optoelectrode, in close proximity to the LED driving circuitry and at high density in order to minimize the size of the device footprint. The high density integration increases mutual capacitance between the traces (Fig. 2b), and in turn makes the electrode circuitry susceptible to EMI resulting from LED driving.

We built models of μLED optoelectrode shanks and calculated the mutual capacitance between the interconnects (Fig. 2c). Because n-type gallium nitride (n-GaN) layer underneath the interconnect is also a part of the LED driving circuitry and its electrostatic potential changes as a function of the LED forward bias voltage, the layer was also taken into account as an electrode in the model. The capacitance between an LED interconnect and a recording electrode interconnect that are the closest with each other was calculated to be 5.37×10^{-19} F μm^{-1}, and that between the n-GaN layer and one recording electrode interconnect was 2.3×10^{-16} F μm^{-1}. If all the interconnects are assumed to be

floating at both ends, capacitive voltage coupling between the LED interconnects and the recording electrode interconnect can be as high as -48.96 dB (3.57 mV coupling for 1 V LED voltage), and the coupling between the n-GaN layer and the recording electrode interconnects can be as high as -0.06 dB (0.99 mV coupling for 1 mV n-GaN voltage). The voltage distribution inside the optoelectrode (and the air surrounding the optoelectrode) is shown in Fig. 2d (top).

In order to effectively reduce capacitive coupling between the LED interconnects and the recording electrode interconnects, the LED interconnects and the recording electrode interconnects were placed into two layers which are separated by a ground-connected metal layer, or the shielding layer, in between (Fig. 2d). In order to prevent coupling from the n-GaN layer, the recording electrode interconnects were places as far as they can be from the edge of the shielding layer directly outside of which the n-GaN is exposed. Electrostatic simulation of the model expected the coupling between the LED interconnect and the recording interconnects and the coupling between the n-GaN layer and the recording interconnects to be reduced by greater than 46 orders of magnitude (to approximately - 975 dB) and 8 orders of magnitude (to approximately - 60 dB), respectively. Because the shielding layer voltage will not be held at strictly zero due to resistive voltage drop through the shank of the optoelectrode and the recording electrodes are electrically connected to electrolyte which is then connected to the ground (as shown in Supplementary Figure 1), actual reduction of EMI-stimulation artifact is expected to be less than that estimated from ideal electrostatic simulation.

We fabricated μLED optoelectrodes with the shielding layer, recorded stimulation artifact resulting from turning on and off μLEDs *in vitro*, and compared the artifact with that recorded on μLED optoelectrodes without the shielding structure (the 1st-generation μLED optoelectrodes). The average peak-to-peak magnitude of the transient artifact and the averaged wideband and high-pass filtered waveforms of the artifact resulting from optical stimulation with 11.5 μW (E_e = 50 mW mm^{-2}) of optical power are shown in Fig. 3. While the magnitude of the artifact did not show any clear correlation to the

amount of optical power generated from the μLEDs on the 1st-generation μLED optoelectrodes (Fig. 3b), that from the shielded μLED optoelectrodes linearly increased with increased amount of generated light (Fig. 3e). At 50 mW mm^{-2}, where the magnitude of the artifact recorded from the shielded device was largest, the reduction of the stimulation artifact was a factor of 5.22. It is clear from the wideband traces (Fig. 3c,f) that most EMI-induced artifact, which is characterized by large-magnitude transient peaking with positive polarity and slow decay, has been greatly reduced.

Reduction of PV-induced artifact with high-density substrate doping

Although the artifact resulting from EMI was greatly reduced with inclusion of shielding layer, when optical stimulation with high intensity was used, the magnitude of the residual artifact was still greater than that of typical spikes (~ 100 μVpp). Interestingly, the polarity of the stimulation artifact that happens right after the beginning and the ending of the LED driving pulses, or the transient artifact, observed from signals from most of the electrodes on the shielded μLED optoelectrodes is negative, unlike the polarity of transient artifact observed on the non-shielded μLED optoelectrodes which is positive (Fig. 3c,f). Inversion of the polarity of the transient artifact suggests that the residual artifact could result from a different source other than EMI, which most likely is coupled through a path that is different from the path through which EMI-induced artifact is coupled.

We confirmed that, by exposing the tips of the optoelectrode to focused LED light with wavelength similar to that of the light generated from the μLEDs ($\lambda \cong 470$ nm), the polarity of the artifact observed on the shielded μLED optoelectrodes is identical to that of the voltage signal that is induced on the signal recorded from the electrodes the on upon illumination (Supplementary Figure 2). We further verified that, by repeating the experiment with electrode array structures fabricated on GaN-on-sapphire GaN/InGaN LED substrate and soda lime glass substrate, the effect is due to neither

PEC nor PV-induced electrostatic potential on GaN layer, but exclusively from a phenomenon taking place inside the silicon substrate (Supplementary Figure 3).

We built a 3D model of a μLED optoelectrode shank and simulated the effect of illumination on the silicon substrate (Fig. 4a). Doping density of boron, an acceptor dopant, inside the silicon substrate and the intensity of the optical illumination were varied. We observed a series of phenomena that results in buildup of electrostatic potential at the substrate-electrolyte interface and in turn generation of a voltage pulse with negative polarity in the recorded signal (Fig 4b). First, optical illumination induces electron-hole pair generation inside the silicon substrate, and the optically generated carriers redistribute inside the substrate separately depending on the type. Difference between electron and hole distribution patterns give rise to electric field inside the substrate, and, in turn, the electrostatic potential of the substrate-electrolyte interface changes. Because the electrolyte is connected to the common reference pin of the amplifier chip which is then connected to the inverting inputs of the low-noise amplifiers in the IC, the resulting output waveform has a negative polarity.

Figure 4c shows expected substrate-electrolyte interface electrostatic potential (voltage) for substrates with different doping densities under illumination with different intensities. It is worth noting that, while higher doping density results in lower voltage at lower irradiance, with higher irradiance, the voltage on lightly doped (typically referred to as p^-) substrate becomes higher than that on substrate that is almost intrinsic (not doped, typically referred to as HR or FZ, especially if the silicon substrate was float-zone grown for high-purity and low doping density). As can be seen in Fig. 3d, it was calculated that the interface voltage from a substrate with boron doping density of 5×10^{16} cm^{-3} (later referred to as p^- substrate) can be as high as that from the substrate with boron doping density of 4×10^{12} cm^{-3} (later referred to as FZ substrate) under illumination with irradiance as high as 50 mW mm^{-2}. On the other hand, the interface voltage from the substrate with boron doping density of 1×10^{20} cm^{-3} (later referred to as p^+ substrate) was kept relatively low even with high intensity illumination.

We fabricated shielded μLED optoelectrodes using GaN-on-Si GaN/InGaN LED wafers with three different boron doping densities and measured the stimulation artifact resulting from driving of LEDs at different intensities. It was first confirmed that there is no significant difference in the electrical and optical characteristics among the μLEDs that were fabricated on wafers with different doping densities (Supplementary Figure 4). As shown in Fig. 5a, stimulation artifact measured from electrodes on shielded μLED optoelectrodes fabricated using LED wafers with FZ silicon substrate and p^- silicon substrate increased with irradiance, whereas that from electrodes on shielded μLED optoelectrodes fabricated using LED wafer with p^+ silicon substrate did not increase with increased irradiance. The average waveforms of the stimulation artifact measured from all the channels that correspond to the electrodes on the tip on which a μLED was turned on are shown in Fig. 5b. It can be seen that, even during LED stimulation resulting with highest intensity (with irradiance of 50 mW mm^{-2} at the surface of the μLED), the magnitude of the stimulation artifact is as low as lower than 200 μVpp, suggesting that PV-induced stimulation artifact has been greatly reduced with heavy doping of the silicon substrate with boron.

Reduction of residual EMI-induced artifact with slew rate modification

Although high-density substrate doping greatly reduced PV-induced stimulation artifact, the average magnitude of the stimulation artifact resulting from high-intensity optical stimulation is still larger than those of typical spikes, which is at most as large as 200 - 300 μVpp. The artifact has to be reduced so that its maximum magnitude is less than the threshold voltage for spike detection, whose typical value is 50 μVpp inside a mouse brain.

Analysis of waveforms of the signals recorded from recording channels that correspond to electrodes at different locations provided a better understanding of the mechanism by which the residual artifact is generated. Fig. 6c shows the average waveforms of stimulation artifact recorded from

the channels that correspond to the electrodes on different locations on the tips of the shielded μLED optoelectrode whose locations are shown in Fig. 6a. Close observation of the pattern of the stimulation artifact reveals that, as can be expected from the mechanism by which it is generated, the PV-induced stimulation artifact, which is characterized by the negative polarity or the 'v'-shape of the transient component, is observed from all the channels with similar magnitude regardless of the location of the electrode. This observation further confirms that the PV-induced stimulation artifact has been eliminated on the shielded μLED optoelectrodes fabricated using LED wafer with p^+ silicon substrate (Fig. 6b). On the other hand, there is a component of the stimulation artifact which has positive polarity (inverted-'v'- or '^'-shaped) and whose magnitude decreases as the distance between the interconnect for the electrode and the μLED that is exposed at the center of the shank through an optical window on the shielding layer increases (Fig. 6d). The polarity and the distance dependence of the stimulation artifact components suggests that this artifact, which is the only residual artifact that can be observed on shielded μLED optoelectrodes fabricated using LED wafer with p^+ silicon substrate, is EMI-induced artifact originating from the μLED that is exposed through an optical window on the shielding layer (Fig. 6e).

Because the magnitude of the residual EMI-induced artifact decreases as the function of the distance of the interconnect from the exposed μLED, it might be possible to reduce the artifact by increasing the average distance between the μLEDs and the interconnects. However, because it is important that the size of the μLED optoelectrode is kept minimal in order to prevent damage induced to the brain tissue, it might not be optimal to move the interconnects away from the LEDs at the cost of larger cross-sectional area.

Because it is not a viable option to further modify the optoelectrode structure to prevent EMI, we decided to manipulate LED driving voltage waveform to reduce the residual EMI. The slew rate, the rate at which the voltage changes when the voltage transitions from a low level (off) to a high level (on),

of the pulse was modified by changing the rise and the fall times of the pulse and changing the low-level voltage. Because LED neither flows significant current nor starts to generate light when biased at voltage lower than the turn on voltage, the low-level voltage can be set as high as 2.8 V. Because change in the rise time affects the frequency from which the higher-order harmonics of the stimulation signal decreases at -40 dB/decade (Supplementary Figure 5), rise time greater than the inverse of the signal recording amplifier's sampling angular frequency ($1 / 2\pi F_s$) would reduce the magnitude of the artifact.

Figure 7 shows the average peak-to-peak magnitude and the waveforms of the stimulation artifact recorded from channels corresponding to the electrodes at the bottom of the tips of shielded μLED optoelectrodes (Fig. 7a), which showed residual EMI-induced artifact with the largest magnitude (Fig. 6d). As expected, rise time longer than 100 μs (0 - 100 % rise time of 125 μs) started to reduce the magnitude of recorded stimulation artifact, resulting in artifact magnitude smaller than 200 μVpp with as long as 1 ms of rise time. Further reduction of artifact magnitude with change of the LED driving signal's low-level voltage level to 2.8 V was confirmed, which effectively reduced the magnitude of the LED driving signal at all frequencies by factor of 5. With 1-ms long rise time and 2.8-V low-level voltage, the average artifact magnitude was 46.53 μVpp, which can be considered artifact-free for applications in which 100 μVpp is used as the spike detection threshold.

Demonstration of artifact-free *in vivo* optoEphys

We validated successful elimination of stimulation artifact from the μLED optoelectrode with inclusion of shielding structure, high-density boron doping of the silicon substrate and slew rate modification *in vivo*. A shielded μLED optoelectrode fabricated using LED wafer with p^+ silicon substrate was implanted into a brain of a mouse and lowered so that its tips are located in the hippocampus (Fig. 8a). Once spontaneous spikes and the characteristic high-frequency oscillations (ripples) were detected from the electrodes, each LED on the shank was turned on with varying intensities to identify the

intensity of optical stimulation at which sufficient light-induce spikes are induced but continuous high-frequency oscillations due to synchronized firing of multiple cells (similar to seizure) is not induced. Rise and fall times of 1 ms were used to ensure maximum reduction of the stimulation artifact without great reduction in the temporal resolution of the optical stimulation. Average stimulation artifact recorded from the channels corresponding to the electrode located on the tip was characterized. With optical stimulation resulting in 2 mW mm^{-2} that induced strong light induced response in many cells (Fig. 8d,e), the average magnitude of the average stimulation recorded from channels corresponding to all the electrode was less than 50 μVpp, as shown in Fig. 8c, with maximum magnitude of 42.02 μVpp on Site 2. Optical stimulation with higher intensity induced seizure inside the region and prevented analysis of stimulation artifact. After characterization of stimulation artifact resulting from driving of each LED, all the three LEDs on the shank were turned with a predefined pattern so that there is a short period during which one LED is turning off, another LED is kept on, and the other LED is turning on (highlighted with a rectangle with black dashed sides in Fig. 8d). As shown in Fig. 8d, the series of optical stimulation with the predefined pattern did not induce any significant stimulation artifact that would prevent either online detection of spikes with naked eyes or offline spike sorting. With offline spike sorting, we identified 8 cells that have distinctive spike waveform. Further analysis of the processed data identified a spike which occurred in the period during which LED 1 and LED 3 were being toggled, as shown in Fig. 8f. As can been seen in Fig. 8g, no noticeable distortion of the spike waveform due to the stimulation artifact was observed, ensuring that the stimulation was artifact-free.

Discussion

While it is possible to reduce the magnitude of stimulation artifact lower than detectable level with slew rate modification, in applications that require fast optical stimulation whose frequency is higher than 1 kHz, it might be not optimal that pulses with rise and fall times as long as 1 ms are used.

While it might not be a solution to modify the optoelectrode structure to further reduce the stimulation artifact, modification of the recording electrode material that would result in lower electrode impedance could potentially help reduce the EMI-induce stimulation artifact. While the relationship between the electrode impedance and the magnitude of the stimulation artifact was not obvious in data recorded using fabricated μLED optoelectrodes due to the small variance of the electrodes' impedance magnitude (Supplementary Figure 6), the circuit model of the optoelectrode suggests that the magnitude of EMI-induced voltage would be lower with lower electrode impedances due to voltage division across the electrode impedance (Supplementary Figure 1). Some post-fabrication techniques such as site-level electrodeposition of conductive micro- and nanoparticles such as Pt nanoparticle and PEDOT:PSS could be utilized to reduce the magnitude of the electrode impedance by a couple of factors and result in consequent reduction of EMI-induced stimulation artifact.

In some applications, it might be more desirable that LEDs are driven with current pulses than with voltage pulses. Current-based LED drivers are be more accessible than the voltage-based drivers, thanks to the easiness of design and implementation using CMOS technology. LED driving of the μLEDs on the μLED optoelectrodes can be thought of LED driving of the μLEDs with voltage pulses with levels that correspond to the current command that is provided to the LED driver. Because of non-zero leakage current from the current driver, the off-level voltage of the LED driving signal would be non-zero, typically just below the LED turn-on voltage. Therefore, driving the LEDs with rectangular current pulses results in generation of the stimulation artifact whose magnitude is similar to that due to driving of the LEDs with rectangular voltage pulses with non-zero low-level voltage. Driving the LEDs with rectangular current pulses with non-zero rise and fall times (or trapezoidal current pulses), although it would result in driving the LEDs with pulses in a different on- and off-time shapes that that of the trapezoidal voltage pulses, did not result in either increment or reduction of the magnitude of the stimulation artifact. We further confirmed that the shape of the current pulses during the pulse on- and off-periods, while it

affects the shape of the stimulation artifact, do not affect the magnitude of the stimulation artifact (Supplementary Figure 7).

Methods

Micro-LED optoelectrode fabrication and device assembly

Micro-LED optoelectrodes were fabricated using microfabrication techniques that are used for fabrication of planar silicon neural probes, also known as Michigan Probes. Simplified device fabrication flow is shown on Fig. 9.

4" silicon wafers with different substrate boron doping densities ($N_A \approx 4 \times 10^{12}$, 5×10^{16}, and 1×10^{20} cm^{-3}, respectively), which have GaN/InGaN multi-quantum-well (MQW) LED layers epitaxial grown with metal-organic chemical vapor deposition (MOCVD) on top, were purchased from Enkris Semiconductors (Suzhou, China). Non-shielded μLED optoelectrodes were fabricated using LED wafers with lightly-boron-doped silicon substrate (p^- silicon substrate, boron doping density of ~ 5×10^{16} cm^{-3}), and the shielded μLED optoelectrodes were fabricated using wafers with all three different boron doping densities.

LED structure, including LED mesas, p- and n-GaN contacts and metallic interconnects, was first formed on the wafer. For the μLED optoelectrodes with shielding layer, additional metal layers were formed by repeatedly passivating the surface of the LED and depositing patterned metal layers. Consecutively, neural signal recording electrodes were formed by passivating the top metal layer and depositing electrode material. Finally, the fabricated μLED optoelectrodes were thinned and released from the silicon wafer by double-sided plasma dicing process.

Released μLED optoelectrodes were assembled on printed circuit boards (PCBs) that provide connections to neuronal signal recording IC and LED driver. The optoelectrode were mounted on printed circuit boards and were electrically connected to the PCBs by wirebonding contact pads on the backend

of the optoelectrode to the gold pads on the PCBs. After potting the exposed wires, connectors (Omnetics Connector Corp., Minneapolis, MN) as well as the ground and the reference wires were soldered to the PCBs.

Characterization of electrical and optical properties of μLEDs

The electrical and optical characteristics of each μLED on the electrodes were characterized before *in vitro* and *in vivo* characterization of stimulation artifact. Both current-voltage (I vs.V) and the irradiance-voltage (E_e vs. V) characteristics were measured for each μLED. First, an optical measurement system consisting of an integrating sphere (FOIS-1, Ocean Optics, Largo, FL) and a spectrometer (Flame, Ocean Optics) were built. A sourcemeter (Keitheley 2400, Keithley Instruments, Cleveland, OH) was then connected across the anode and the cathode pins of an μLED on the connector. The tips of the optoelectrode were lowered so that the whole shanks are inside the integrating sphere, ensuring that all the light generated from the μLED can be collected. The DC voltage across the LED anode and the cathode terminals were swept from 0 V to 4 V, and the resulting current and the spectral flux of the μLED was measured. The radiant flux was calculated by integrating the spectral flux over wavelengths from 350 nm to 600 nm, and the irradiance on the surface of the μLED was then calculated by dividing the radiant flux by the area of the μLED's active region (230 μm^2).

***In vitro* characterization of LED-driving-induced artifact**

All *in vitro* characterization were conducted in 1 × phosphate buffered saline (PBS) solution (prepared using 10 × PSB purchased from MP Biomedicals, Solon, OH). A puddle of PBS was prepared by pouring approximately 100 mL of 1 × PBS solution into a small petri dish. The μLED optoelectrode was lowered into the puddle so that approximately half of the shank (the lower half of the shanks including

the tips, ~ 2.5 mm) was submerged into the PBS. The exposed stainless steel tips at the loose ends of the ground and the reference wires were also submerged into the PBS.

A miniature neural signal amplifier headstage PCB (RHD2132, Intan Technologies, Los Angeles, CA), in combination with a recording system (RHD2000, Intan Technologies), recorded the stimulation artifact signal, while a function generator (33220A, Keysight Technologies, Santa Rosa, CA) provided voltage pulses for LED driving. First, magnitude and the phase of each recording electrode's impedance at 1 kHz were measured using the Intan amplifier.

50-ms long (5 Hz frequency, resulting in 25 % duty ratio) rectangular voltage pulses with varying off- (low-level) and on-time (high-level) voltage levels and pulse rise and fall times were used as the LED driving signal. For stimulation sequences whose rise and fall times are not specified, 5-ns rise and fall times were used. For simulation sequences whose irradiance instead of voltage levels were reported, a voltage corresponding to the LED forward bias voltage that generates the irradiance same as the pre-characterized irradiance was used as the high-level voltage, and 0 V was used as the low-level voltage. Typically, high-level voltages of 3.5 - 3.7 V were used for 50 mW mm^{-2} irradiance. For characterization of the effect of slew rate on the magnitude of the stimulation artifact, in order to eliminate the effect of the PV-induced stimulation artifact, only the shielded μLED optoelectrode fabricated using the LED wafer with p^+ silicon substrate were used.

For each experimental condition for each μLED, signals from the input channels of the neural signal amplifier IC were recorded for 30 seconds, so that artifact signals from longer than 100 pulses can be recorded. Average artifact signal was calculated by first high-pass filtering the signal to remove low-noise fluctuations (with filters with 10 Hz and 250 Hz cutoff frequencies for wideband signal and high-pass filtered signals, respectively) and calculating the average of the middle 200-ms long segments (50 total segments out of ~ 100 recorded segments) after the first 5 s of the recorded signal. Transient artifact magnitude was calculated from the difference between the maximum and the minimum values

of high-pass filtered signal during the first 5-ms period from the point when the voltage changed from the off-level for pulses. The average transient artifact magnitude was calculated by averaging the values from electrode whose impedance magnitudes are between 500 MΩ and 2 MΩ and the phases are between -80 ° and -55 ° at 1 kHz. Two optoelectrodes from each cohort was used, and at least 21 electrodes per optoelectrode (out of 32 total, 25.83 in average) contributed to calculation of the average artifact magnitude. The average 1 kHz magnitude and phase of the electrode impedance of the electrodes which contributed to calculation of the average artifact magnitude were 1.09 ± 0.09 MΩ and -68.2 ± 4.9 ° (mean ± SD).

***In vivo* characterization and demonstrations of stimulation-artifact-free optoEphys**

The animal procedures were approved by the Institutional Animal Care and Use Committee of the University of Michigan (protocol number PRO-7275). One male C57BL/6J mouse (32 g) was used for *in vivo* characterization. The mouse was kept on a regular 12 h - 12 h light - dark cycle and housed in pairs before surgery. No prior experimentation had been performed on this animal. Atropine (0.05 mg/kg, s.c.) was administered after isoflurane anesthesia induction to reduce saliva production. The body temperature was monitored and kept constant at 36 - 37 °C with a DC temperature controller (TCAT-LV; Physitemp, Clifton, NJ, USA). Stages of anesthesia were maintained by confirming the lack of nociceptive reflex. Skin of the head was shaved and the surface of the skull was cleaned by hydrogen peroxide (2 %). A 1-mm diameter craniotomy was drilled at 1.5 mm posterior from bregma and 2 mm lateral of the midline. The dura was removed over the dorsal CA1 region of the hippocampus and the mouse was injected with AAV5, CaMKII promoter driven ChR2 (AAV5-CaMKIIa-hChR2(H134R)-EYFP), resulting in expression of ChR2 in pyramidal neurons. Viruses were purchased from the University of North Carolina Vector Core (UNC-REF). After the surgery, the craniotomy was sealed with Kwik-Sil (World Precision Instruments, Sarasota, FL) until the day of recording.

On the day of recording, the mouse was anesthetized with isoflurane, the craniotomy was cleaned, and a shielded μLED optoelectrode with p^+ silicon substrate was lowered to the CA1 region of the hippocampus. Baseline recording was performed (30 min), after which simultaneous recording and stimulation were done using three μLEDs from one shank (as described in Results in more details). 0.46 μW power, equivalent to 2 mW mm-2 irradiance at the surface of each μLED, was used to characterize the light induced artifact *in vivo* and to alter the activity of neurons (more details are provided in Results). For characterization of stimulation artifact and confirmation of optical induction of neuronal activities, Pulsed optical stimulation (100-ms long, 2 Hz, 100 pulses) was generated from each μLED. The (10 - 90 %) rise and the fall times of each voltage pulse were set as 1 ms. After collecting sufficient data using optical stimulation from each μLED, a 500-ms long optical stimulation sequence involving switching on and off all the three μLEDs on the shank (whose details are provided in Results) were repeated 100 times. RHD2132 miniature neural signal amplifier headstage and RHD2000 recording system were used for acquisition of data from all the recording electrodes (n = 32). Keysight 33220A function generator provided voltage pulses for LED driving.

A custom MATLAB (MathWorks, USA) script was used to calculate average stimulation artifact. The wideband traces were first high-pass filtered with a first-order filter with 250 Hz cutoff frequency to remove low-noise fluctuations. The average artifact signal from each recording channel was then obtained by averaging the middle 500-ms long segments (90 total segments out of 100).

The recorded data were then further analyzed for identification and sorting of action potentials. No manipulation in data (e.g. trimming of 1-ms long segments before and after the beginning and the ending of each pulsed optical stimulation) other than high-pass filtering (at 500 Hz) of the baseband signal were conducted. Spikes were first detected and automatically sorted using the Kilosort algorithm [Pachitariu 2016] and then manually curated using Phy to get well-isolated single units (multi-unit and noise clusters were discarded). To measure the effect of LED stimulation on neuronal activity,

peristimulus time histograms (PSTHs) were built around stimulus onset (spike trains were binned into 10-ms bins). Baseline and light-induced firing rate were calculated for each single unit, in which the baseline was defined as light-free epochs (400 ms) between trials and the stimulation period as the light-on (100 ms). Wilcoxon-signed rank test was used to compare the mean firing rate per trial (n = 100 trials) during baseline and LED stimulation.

Figures

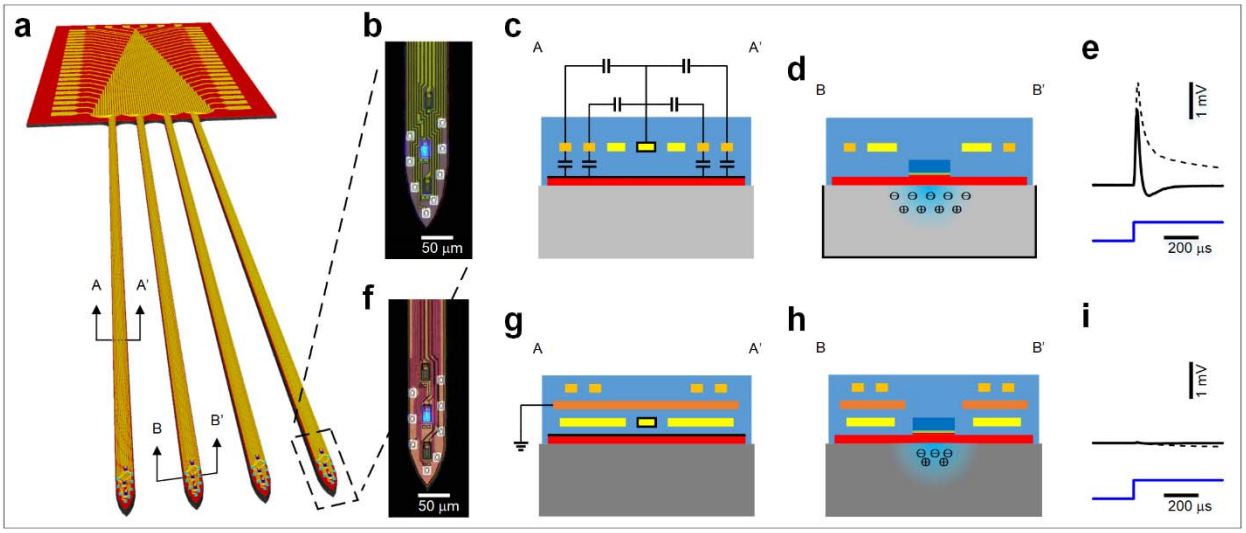

Figure 1: Micro-LED optoelectrode, sources of stimulation artifact, and stimulation artifact reduction schemes. (a) Schematic illustration of a (1st-generation) µLED optoelectrode. (b) Microphotograph of a tip of the 1st-generation µLED optoelectrode. Eight recording electrodes, three µLEDs, and interconnection lines that connect the electrodes and the µLEDs to the optoelectrode backend are shown. (c) Cross-sectional schematic diagram of a shank of the first-generation µLED optoelectrode, showing sources of the electromagnetic interference (EMI) in black bold lines. (d) Cross-sectional schematic diagram of a tip of the 1st-generation µLED optoelectrode, showing optical generation of carriers and photovoltaic-effect(PV)-induced electrostatic potential at the substrate-electrolyte interface. (e) An example stimulation artifact recorded from a channel of the 1st-generation optoelectrode. Wideband signal is shown in black dashed line, high-pass filtered signal in black solid line, and LED input signal in blue solid line. (f) Microphotograph of a tip of the second-generation µLED optoelectrode on which stimulation artifact reduction schemes are implemented. (g-h) Cross-sectional schematic diagrams of the shank (part g) and the tip (part h) of the second-generation µLED optoelectrode, showing methods for reduction of stimulation artifact: shielding layer and high-density

doping of the substrate, respectively. (i) An example stimulation artifact recorded from a channel of the second-generation optoelectrode. The color scheme is identical to that of part e.

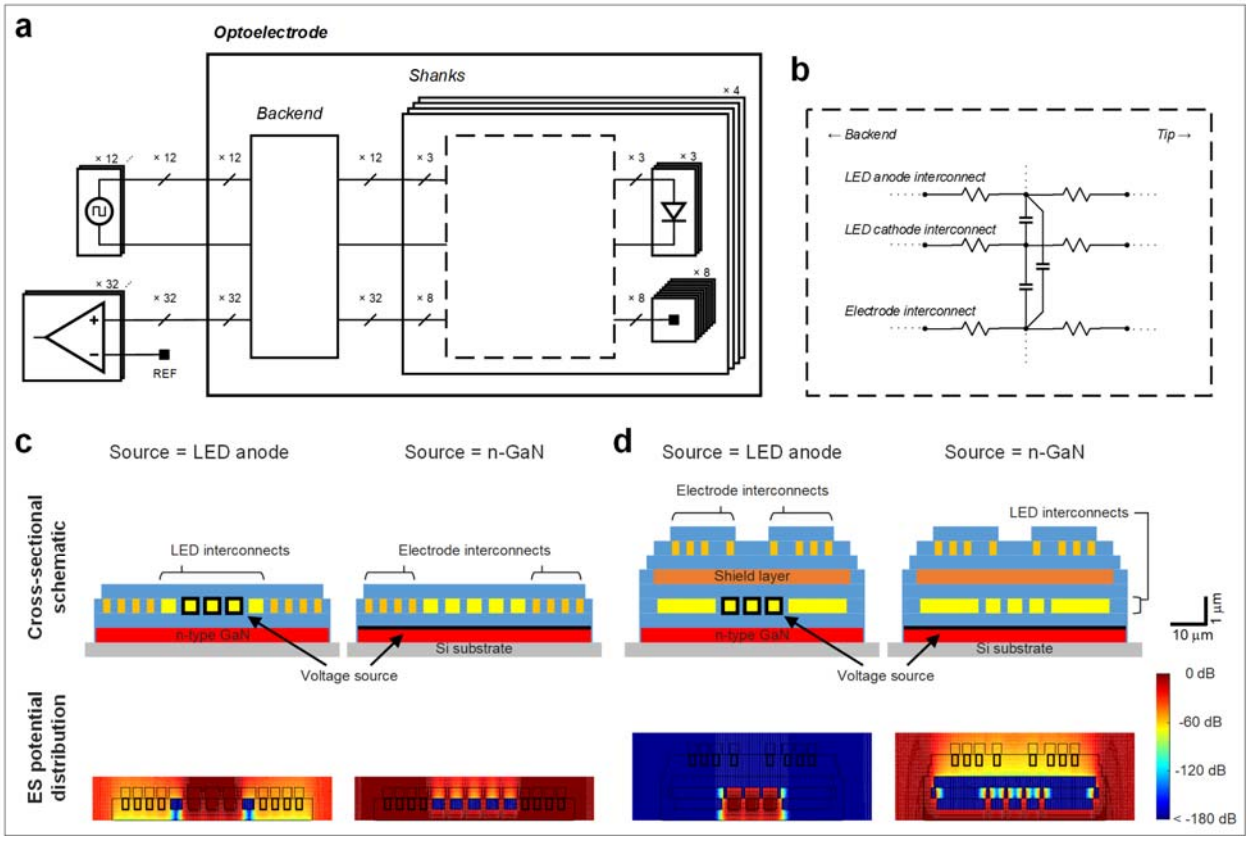

Figure 2: Generation of EMI-induced stimulation artifact. (a) System-level electrical circuit schematic diagram of a µLED optoelectrode, a LED driving system, and a neural signal recording system. Some details are omitted for better visibility, including some resistors representing the line and the contact resistances. The equivalent circuit of the backend, which is similar to that of the shank shown in part b, is also omitted. (b) Simplified electrical circuit schematic diagram of a shank of the µLED optoelectrode. Only one of each type of interconnect is shown for better visibility, and the inductors were ignored due to their small values. The complete electrical circuit model of the shank consists of multiples of the unit cells shown in the diagram in the form of a T-network. (c) Results of finite-element-method (FEM) simulation of the electrostatic potential distribution inside the non-shielded (1st-generation) optoelectrode shank cross-section due to voltage from different EMI sources. In the schematic illustrations of the shank cross-sections of the µLED optoelectrodes, yellow rectangles indicate LED anode and cathode interconnects, gold rectangles recording electrode interconnects, red rectangles LED

(n-GaN and In(Ga)N buffer) layer, and grey rectangles silicon substrate. Regions in light blue indicate silicon dioxide insulators. Sources of EMI are highlighted with bold black lines. Electrostatic potentials of the highlighted regions were set as 1 V, while those of the other parts of the LED driving circuitry were set as 0 V. (d)) Results of finite-element-method (FEM) simulation of the electrostatic potential distribution inside the shielded optoelectrode shank cross-section due to voltage from different EMI sources. The color schemes identical to the one used in part c were used, while an additional color, orange, was used to indicate the shielding layer in the schematic diagram. Great reduction of the electrostatic potential with the additional shielding layer, which also indicates reduction of the mutual capacitance, is visible for both the fields originating from the LED anode interconnects and that originating from the n-GaN layer.

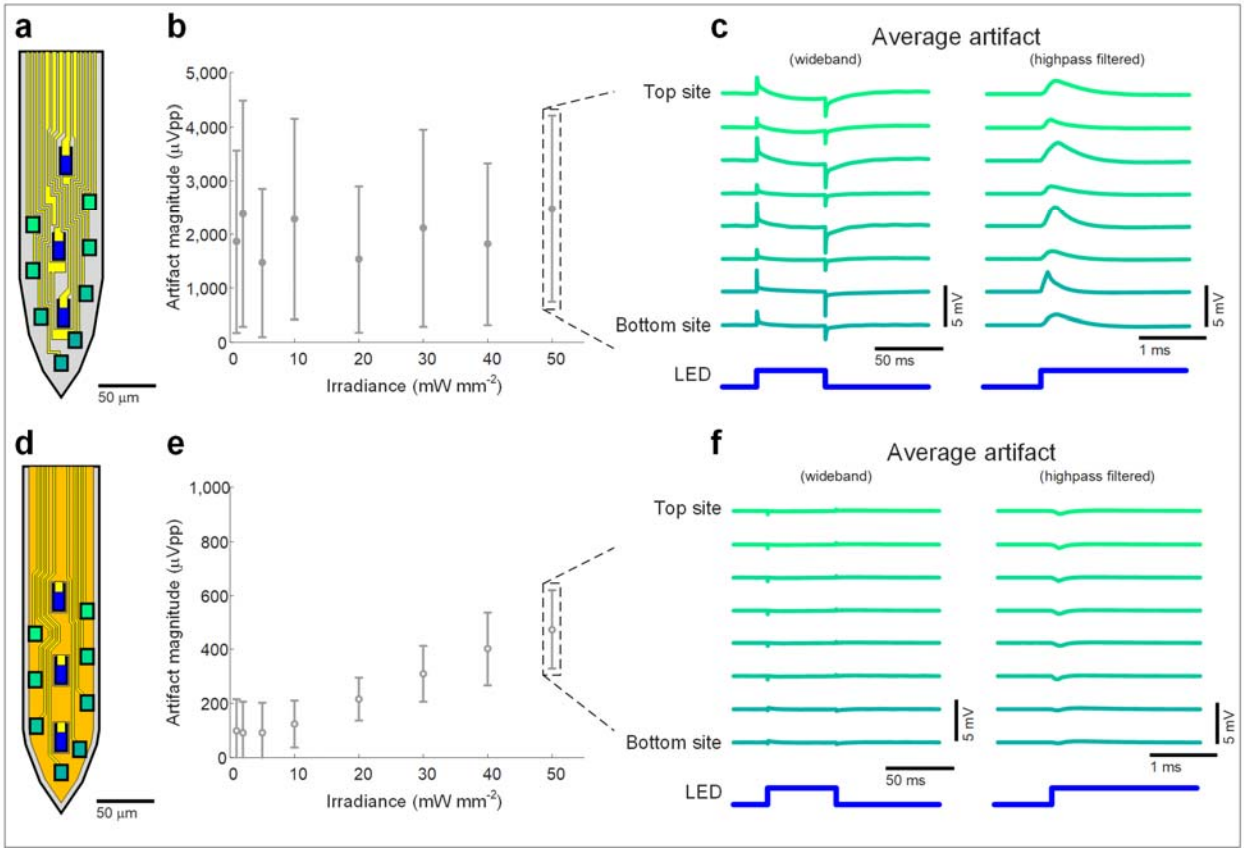

Figure 3: Reduction of EMI-induced stimulation artifact with inclusion of shielding layer. (a) Schematic illustration of the tip of a non-shielded (first-generation) µLED optoelectrode. Blue rectangles indicate LEDs and the yellow polygons indicate metal interconnects. Recording electrodes are indicated with rectangles with bold black sides. The face color of each electrode-indicating rectangle corresponds with the line color of the trace indicating the signal recorded from the recording channel corresponding to the same electrode in part c. (b) Average peak-to-peak magnitude of the high-pass filtered stimulation artifact recorded from the channels on the non-shielded µLED optoelectrodes corresponding to the electrodes on the shank on which a µLED was turned on. X coordinate indicate the irradiance at the surface of the µLED. Error bars indicate one standard deviation. (c) Waveforms of stimulation artifact recorded from the channels that correspond to the electrodes on different locations on the tips of the non-shielded µLED optoelectrode when LED driving signal with resulting irradiance of 50 mW mm-2 at the surface of the µLED was used. The blue trace at the bottom indicate the LED signal. Resemblance

between the waveform of the stimulation artifact and that of the LED signal indicates strong EMI coupling. (d) Schematic illustration of the tip of a shielded μLED optoelectrode. The color scheme identical to that of part a was used, except for an additional color, gold, to indicate the shielding layer. (e) Average peak-to-peak magnitude of the high-pass filtered stimulation artifact recorded from recording channels on the shielded μLED optoelectrodes. (f) Waveforms of stimulation artifact recorded from the channels that correspond to the electrodes on different locations on the tips of the non-shielded μLED optoelectrode. The discrepancy between the LED signal (blue trace at the bottom) and the recorded signal indicate elimination of EMI-induced stimulation artifact.

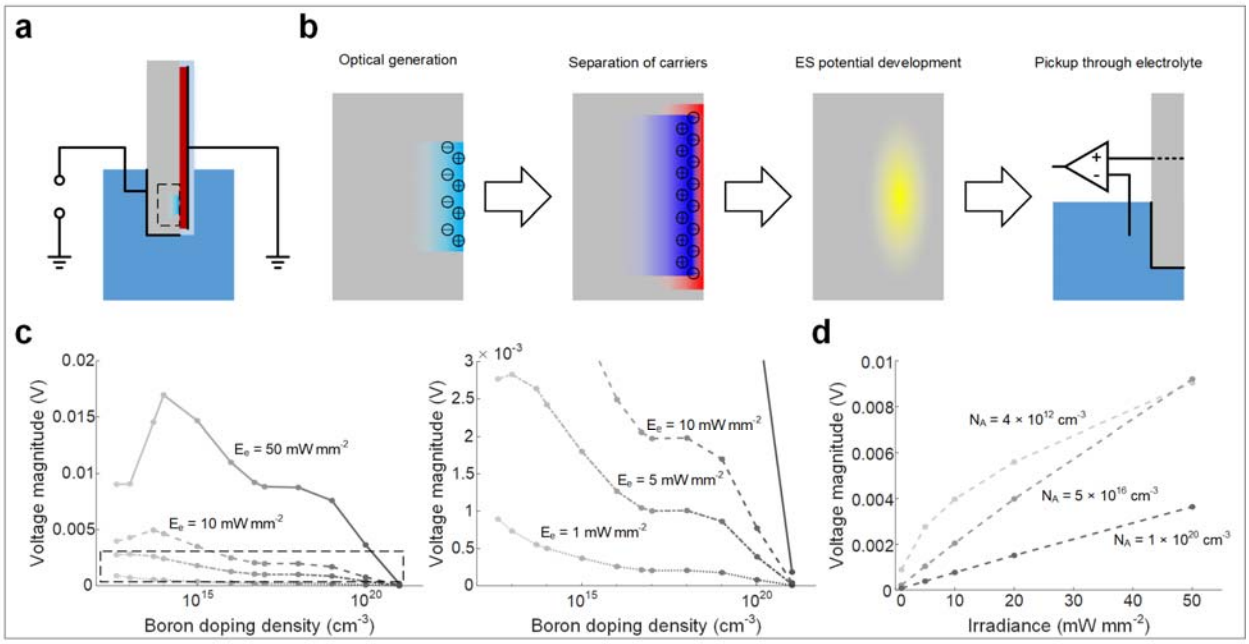

Figure 4: Generation of photovoltaic (PV)-effect-induced electrostatic potential and consequent stimulation artifact. (a) Schematic illustration of the cross-section of the 3D model used in the finite-element-method device physics simulation. Grey rectangle indicates boron-doped silicon, red rectangle AlN buffer, light blue region silicon dioxide insulator. The electrolyte, which the darker light blue region surrounding the bottom half of the μLED optoelectrode indicates, was not included in the model but was taken into account by applying a boundary condition to the electrode at the interface. Bold black lines indicate the electrodes in the model and their boundary conditions. (b) Schematic illustrations of the processes through which electrostatic potential is induced and PV-induced stimulation artifact is generated. The first three panels are the magnified views of the region inside the rectangle with the black dashed sides on part a. Circles with plus signs indicate holes, circles with minus signs electrons, shading in light blue optical generation, shading in blue distribution of holes, shading in red distribution of electrons, and shading in yellow electrostatic potential. In the steady state, all the processes occur simultaneously and in turn maintains a steady distribution of the electrostatic potential inside the substrate. (c) Steady-state voltage of the electrode representing the substrate-electrolyte interface, calculated at different doping densities and light intensities. The right panel shows the magnified view of

the region inside the rectangle with black dashed sides on the left panel. (d) Steady-state substrate-electrolyte interface voltage of substrates with a few selected boron doping densities at different light intensities. The voltage from heavily boron-doped silicon substrate stays low even at higher irradiance, which that from intermediately boron doped silicon substrate increases and exceeds that from very lightly doped silicon substrate, suggesting great reduction of the PV-induced stimulation artifact with higher boron doping.

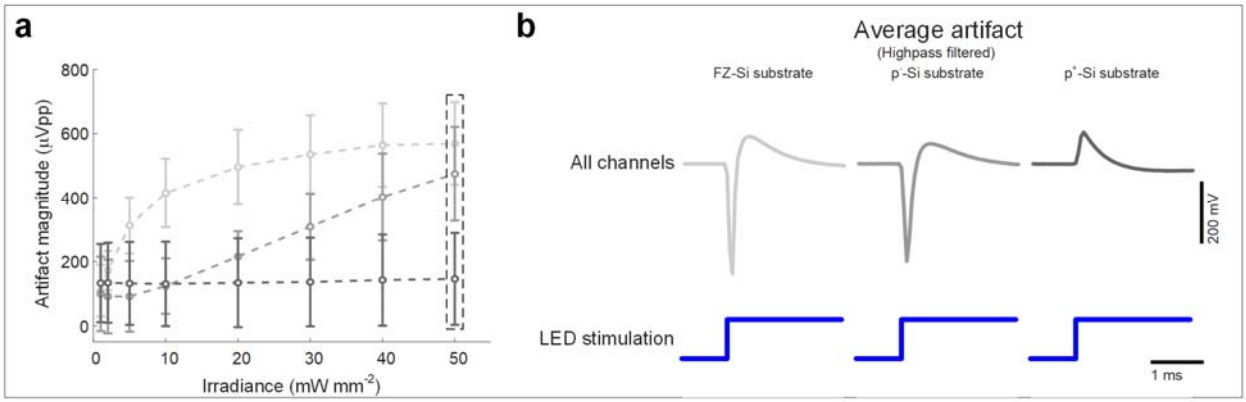

Figure 5: Reduction of PV-induced stimulation artifact with heavy boron doping of silicon substrate. (a) Average peak-to-peak magnitude of the high-pass filtered stimulation artifact recorded from recording channels on the shielded μLED optoelectrodes corresponding to the electrodes on the shank on which a μLED was turned on. Darker color indicate higher boron doping density. X coordinate indicate the irradiance at the surface of the μLED, and the error bars indicate one standard deviation. (b) Average high-pass filtered waveforms of stimulation artifact recorded from the channels that correspond to the electrodes on the shank on which a μLED was turned on. LED driving signal with resulting irradiance of 50 mW mm^{-2} at the surface of the μLED was used. The blue traces at the bottom indicate the LED signal. The sharp transient component with negative polarity is eliminated on the shielded μLED optoelectrode fabricated using the wafer with heavily boron-doped silicon substrate.

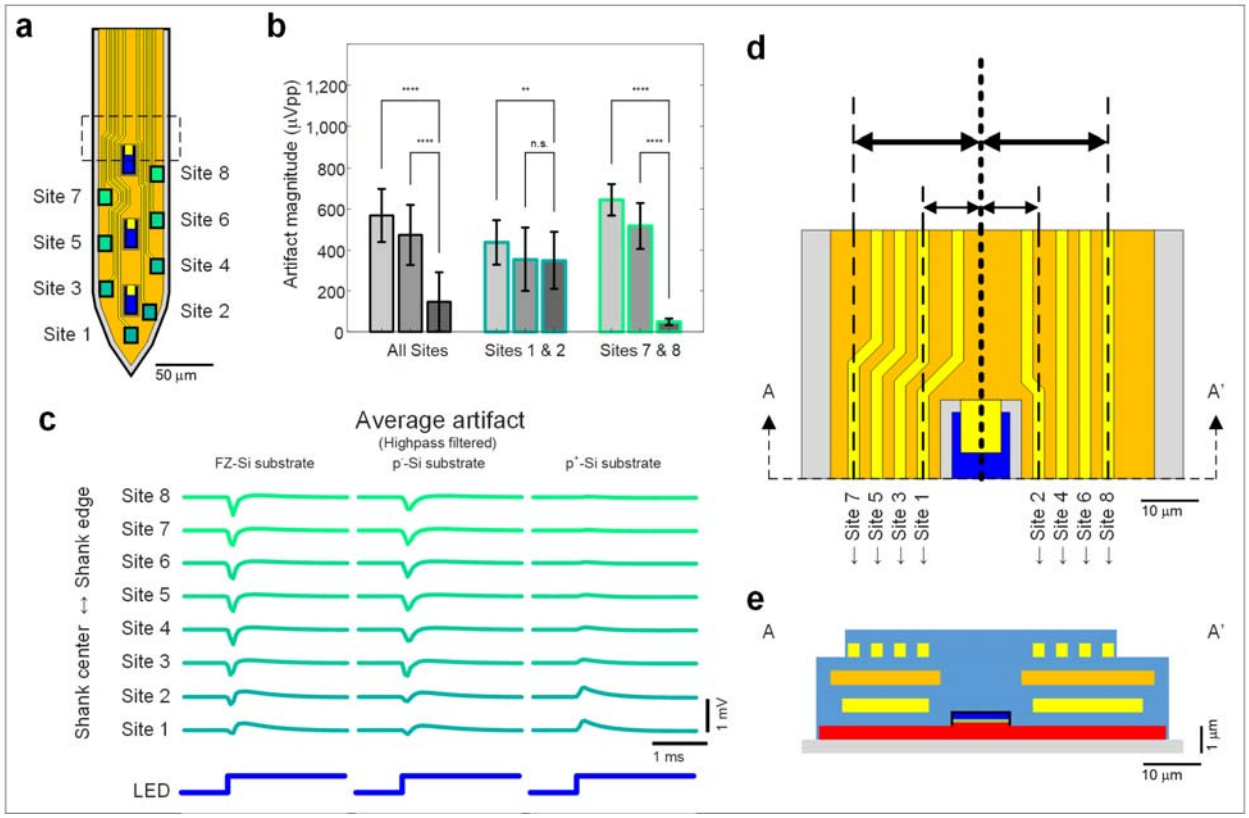

Figure 6: Residual EMI-induced stimulation artifact. (a) Schematic illustration of the tip of a shielded µLED optoelectrode. The color scheme is identical to that of Fig. 3d. (b) Average peak-to-peak magnitude of the high-pass filtered stimulation artifact recorded from the channels on the shielded µLED optoelectrodes corresponding to the electrodes on the shank on which a µLED was turned on. LED driving signal with resulting irradiance of 50 mW mm^{-2} at the surface of the µLED was used. The face color of each bar indicates boron doping density of the silicon substrate on which the µLED optoelectrode is built, darker color indicating higher doping density. Error bars indicate one standard deviation. Wilcoxon rank-sum test was used, n.s. indicates $p > 0.05$, ** indicates $0.001 < p < 0.01$, and **** indicates $p < 1 \times 10^{-4}$. Elimination of artifact on the Sites 7 and 8 on the µLED optoelectrode with p^+ silicon substrate is notable. (c) Waveforms of average stimulation artifact recorded from the channels that correspond to the electrodes on different locations on the tips of the shielded µLED optoelectrode. LED driving signal with resulting irradiance of 50 mW mm^{-2} at the surface of the µLED was used. The

color scheme is identical to that of Fig. 3f. (d, e) Magnified top view (part d) and the cross-sectional view (part e) of the region inside the rectangle with the black dashed sides on part a. The distance between the center of the interconnect and the center of a μLED, which is exposed through an optical window on the shielding layer, is shown for a few selected recording electrode interconnects. While the magnitude of the transient component of the stimulation artifact whose polarity is negative (v-shaped) does not change as the function of the distance between the μLED and the interconnect, the magnitude of the component whose polarity is positive (^-shaped) decreases as the distance increases. The distance dependent of the artifact magnitude suggests that the source of the residual artifact that remains on the shielded μLED optoelectrode fabricated using heavily-boron-doped silicon wafer is EMI originating from the μLED exposed through the optical window.

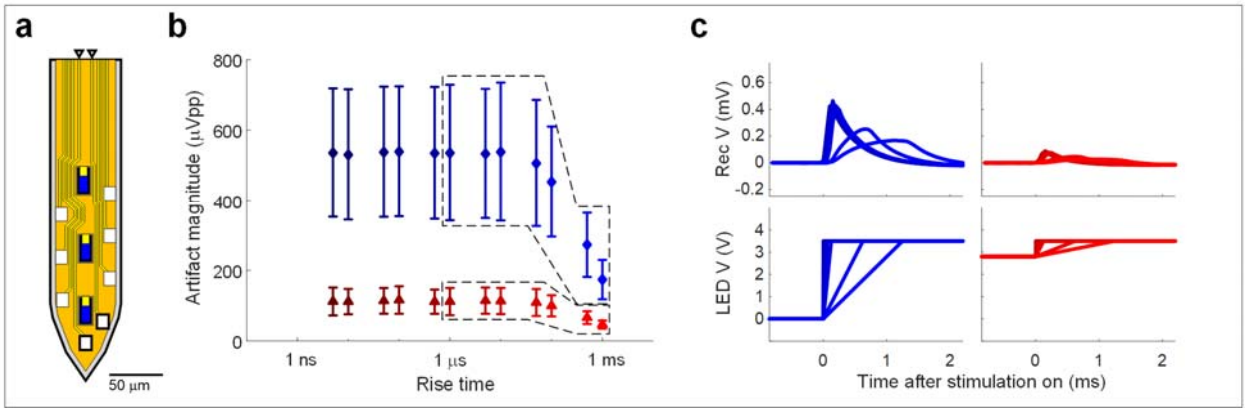

Figure 7: Reduction of residual EMI-induced stimulation artifact with slew rate modification. (a) Schematic illustration of the tip of a shielded µLED optoelectrode with heavily boron-doped silicon substrate. The locations of the electrodes and the interconnects from which the signals were recorded are indicated with rectangles with bold black sides and black arrowheads, respectively. (b) Average peak-to-peak magnitude of the high-pass filtered stimulation artifact recorded from the channels on the µLED optoelectrodes on the shank on which a µLED was turned on. X coordinate indicate the 10 - 90 % rise time of the pulse. Blue color indicates that the voltage pulses used as the LED input signal had zero low-level (off-time) voltage, and the red LED non-zero low-level voltage. Error bars indicate one standard deviation. (c) Average waveforms of the recorded stimulation artifact and the input voltage signal. Significant reduction of the stimulation artifact with slew rate modification is visible.

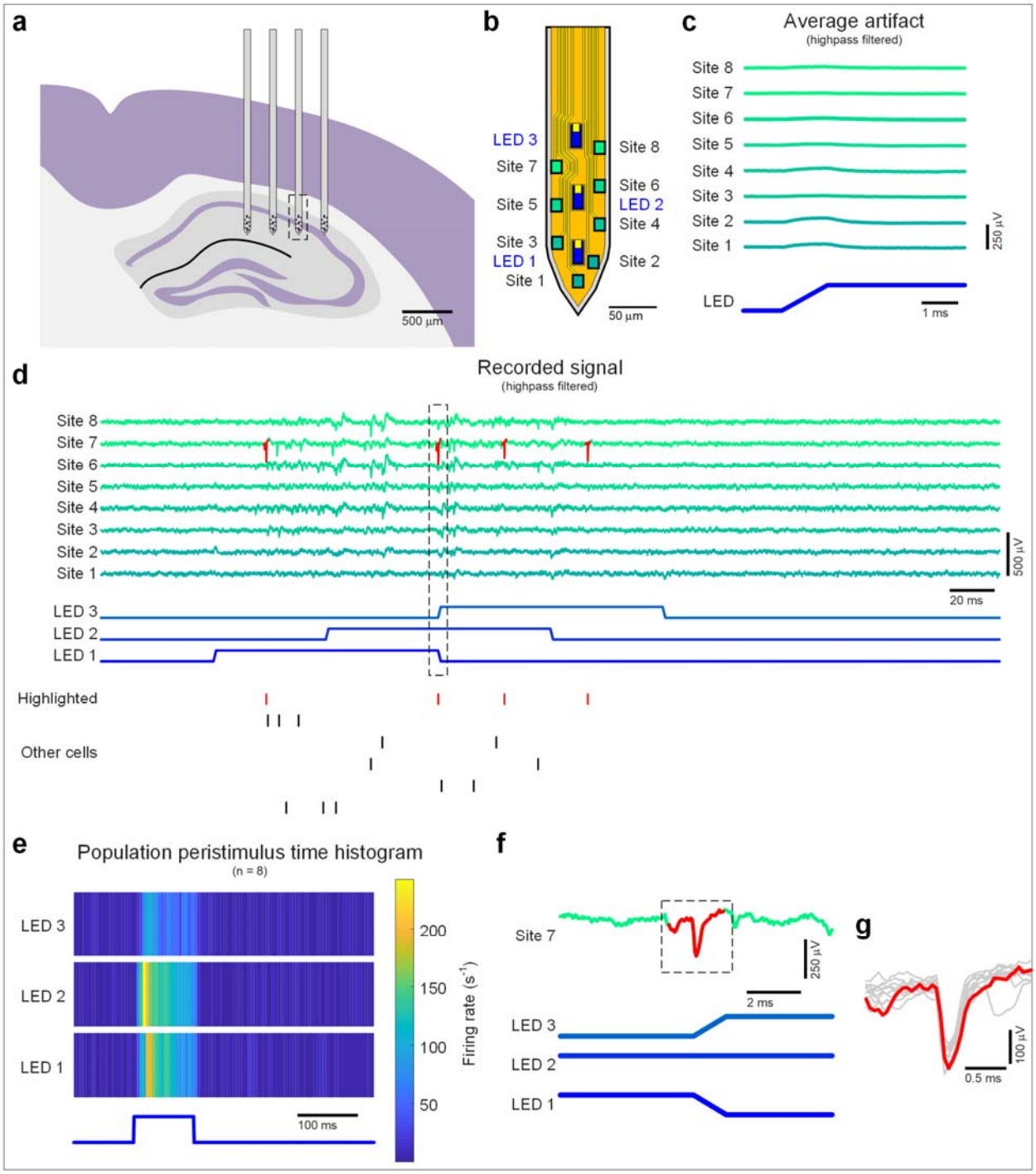

Figure 8: Demonstration of stimulation-artifact-free *in vivo* optoEphys. (a) Schematic illustration of the relative location of the µLED optoelectrode inside the brain. The shank from which the data presented in parts b-g were collected is highlighted with a rectangle with dashed sides. (b) Schematic illustration of the tip of a shielded µLED optoelectrode. The color scheme is identical to that of Fig. 3d, except for

different LED face colors indicating LEDs at different locations. (c) Waveforms of stimulation artifact recorded from the channels that correspond to the electrodes on different locations on the tips of the shielded μLED optoelectrode. Clear elimination of stimulation artifact ($V_{peak\text{-}to\text{-}peak} < 50\ \mu V$) is shown on all the recording channels. (d) Traces of the recorded signals and the raster plots of the sorted spikes. Strong light-induced activities and lack of stimulation artifact on all the recording channels are shown. The color scheme for the recorded signal traces are identical to that in Fig. 3d. (e) Peristimulus time histograms of the cells that were identified from the recorded signals whose traces are shown in part d. Induced activities are clearly visible during the stimulation on-time. (f) Magnified view of the traces of the signal recorded from Site 7 and the signals provided to the LEDs inside the region highlighted with a rectangle with black dashed line in part d. No distortion of the recorded signal during the short period within which two LEDs were simultaneously toggled is shown. (g) Magnified view of the spike inside the region highlighted with a rectangle with black dashed line in part f overlaid on top of waveforms of ten spikes from the same unit that were observed before and after spike highlighted in red, showing no distortion of the spike waveform.

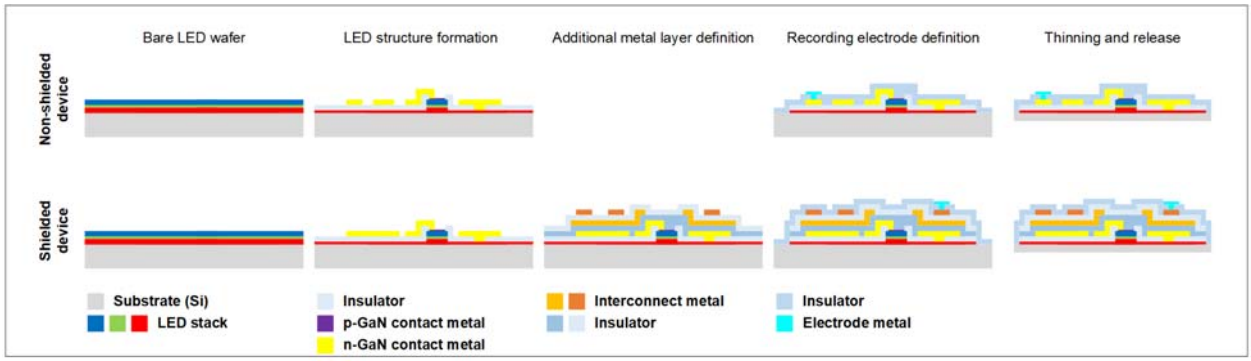

Figure 9: Micro-LED optoelectrode fabrication process flow. An imaginary cross-section containing only one LED and one recording electrode are located at is shown for each type of µLED optoelectrode.

References

[Buzsaki 2004] G Buzsaki, “Large-scale recording of …,” Nat. Neurosci 2004

[Boyden 2005] E Boyden et al., “Millisecond-’, Nat. Neurosci 2005

[Deisseroth 2011] K Deisseroth et al., “Optogenetics,” Nat. Methods 2011

[Buzsaki 2015] G Buzsaki et al., “Tools for probing …,” Neuron 2015

[Wise 1975] Wise et al., "A Low-Capacitance …”IEEE TBME 1975

[Wise 2008] Wise et al, “Microelectrodes, …” IEEE 2008

[Wu 2013] F Wu et al., “An implantable neural …,” J. Neural Eng. 2013

[Kampasi 2016] K Kampasi et al., “Fiberless multicolor neural …,” Sci. Rep. 2016

[Wu 2015] Wu et al., "Monolithically Integrated muLEDs …” Neuron 2015

[English 2017] D English et al., “Pyramidal cell-interneuron circuit …,” Neuron 2017

[Kim 2016] K Kim et al, “GaN-on-Si …,’ IEDM 2016

[Grosenick 2015] L Grosenick et al, “Closed-loop and Activity-Guided …,” Neuron 2015

[Wise 1970] K Wise et al., “An integrated-circuit approach …,” IEEE TBME 1970

[Royer 2010] S Royer et al., “Multi-array Silicon Probes …,” Eur. Jour. Neurosci. 2010

[Mikulovic 2016] S Mikulovic et al., “On the photovoltaic …,” Neurophotonics 2016

[Jun 2017] J Jun et al., “Fully integrated silicon …,” Nature 2017

[Kampasi 2018] K Kampasi et al., “Dual color optogenetic …,” Microsystems & Nanoengineering 2018

[Ayling 2009] O Ayling et al., “Automated light-based mapping …,” Nat. Methods 2009

[Han 2009] X Han et al., “Millisecond-Timescale optical control …,” Neuron 2009

[Cardin 2010] J Cardin et al., “Targeted optogenetic stimulation …,” Nat. Proc. 2010

[Khuram 2013] A Khurram et al, “Investigation of the …,” Prof. IEEE EMBS 2013

[Laxpati 2014] N Laxpati et al., “Real-time in vivo …,” Frontiers in Neuroengineering 2014

[Budai 2018] D Budai et al., “A novel carbon …,” PLoS ONE 2018

[Kuzum 2014] D Kuzum et al., “Transparent and flexible …,” Nat. Comm. 2014

[Park 2016] D Park et al., “Fabrication and utility …,” Nat. Protocol 2016

[Scholvin 2016] J Scholvin et al, “Closed-packed silicon microelectrodes …,” IEEE TBME 2016

[Pachitariu 2016] M Pachitariu et al, “Kilosort: …,” bioRxiv 2016

Acknowledgements

K. K. acknowledges support from NSF#1545858 and NSF#1707316.

Author Information

Affiliations

Department of Electrical Engineering, University of Michigan, Ann Arbor, Michigan 48105, USA

Kanghwan Kim, Mihály Vöröslakos, John P. Seymour, Kensall D. Wise & Euisik Yoon

Neuroscience Institute, Langone Medical Center, New York University, New York, NY, 10016

Mihály Vöröslakos & György Buzsáki,

Author contributions

K. K. design, fabricated, and assembled μLED optoelectrodes; designed and conducted *in vitro* characterizations; designed and participated in *in vivo* experiments; conducted CAD simulations; conducted analyses of stimulation artifact of recorded data both *in vitro* and *in vivo*; prepared figures; and wrote the manuscript with input from the other authors. M. V. conducted *in vivo* experiments and processed recorded neuronal signals. J. S., K. D. W., G. B. and E. Y. supervised the project, contributed to design of experiments and editing the manuscript.

Corresponding author

Correspondence to Euisik Yoon